

Quantum-wire exciton dispersion in a multiband real-space scheme

Anastassios Siarkos and Erich Runge

Institut für Physik, Humboldt-Universität zu Berlin, Hausvogteiplatz 5-7, 10117 Berlin, Federal Republic of Germany

(Received 6 March 2000)

Numerical multiband calculations of quantum-wire excitons including valence-band $\mathbf{k}\cdot\mathbf{p}$ coupling and going beyond the idealization of a circular or rectangular wire cross section are presented. These are based on a real-space formulation. For a specific GaAs/Al_xGa_{1-x}As V-groove quantum wire, results are shown for the exciton dispersion, the kinetic exciton mass, the dependence of the exciton wave function on the center-of-mass momentum, and the polarization anisotropy of the excitonic absorption.

I. QUANTUM-WIRE EXCITONS

For semiconductor quantum wells (QW) and quantum wires (QWR), it has been well known for a long time that excitons dominate the optical properties near the fundamental band edge at low temperatures and remain important even at room temperature. Not surprisingly, a steady stream of papers calculating QW excitons at vanishing center-of-mass (COM) momentum, $Q=0$, with improving accuracy and insight was seen over the past fifteen years. Much less has been done regarding QW excitons at finite momentum¹⁻⁴ and even less for QWR excitons. For QWR, all published work on optical spectra (i) used drastically simplified models for the underlying single-particle bands,⁵⁻⁸ (ii) considered highly idealized geometries,⁹ or (iii) treated the Coulomb interaction only approximately.⁹⁻¹⁵ The first group typically ignored the multiband character of the valence-band maximum. The last group either ignored the Coulomb interaction completely,^{10,11} added it as a rigid shift of all states at a final stage,^{12,13} approximated it by a one-dimensional form,⁹ or, in the best case, used a Hartree approximation.^{14,15} In the latter, each constituent of the exciton reacts to the charge distribution of the other one, but correlations between both particles are neglected. For QWR, again, work has been focused on properties of the exciton at rest, $Q=0$.

The internal structure of the ground-state exciton, i.e., the relative motion of electron and hole, determines, among others, the binding energy and the polarization dependence of its absorption. Aspects of the COM motion enter the exciton's localization properties, its energy relaxation, and, via the exciton dispersion $\epsilon_x(Q)$, the exciton density of states and their occupation. These, in turn, determine the behavior of possible QWR-based optoelectronic devices. Indeed, the absence of an energy shift with increasing excitation density has been attributed to direct involvement of excitons in QWR lasing.^{16,17} However, early expectations that QWR devices would profit from the diverging one-dimensional density of states had to be revised due to excitonic correlations reducing the spectral density considerably.^{14,18-20} Nevertheless, understanding excitons in a QWR remains a challenge, and remarkable effects have been predicted such as an exciton crystal in finite-length QWR.²¹

A particularly important aspect of the exciton dispersion is the kinetic COM mass. For the typically strongly nonparabolic exciton dispersions in low-dimensional structures,

there is, of course, no unique definition of a "mass." There is, thus, some uncertainty about what mass parameter should actually be used for different processes like exciton formation and thermalization,² exciton localization,²² and the exciton-photon interaction (polaritons).¹

This paper presents the first accurate results on the exciton dispersion in a realistic QWR, including both the degenerate valence-band structure and the Coulomb correlation. The exciton Schrödinger equation was solved in real space, with the Hamiltonian

$$H = H_e + H_{\text{Lutt}} + V_{\text{conf}}^{(e)} + V_{\text{conf}}^{(h)} + W_{\text{Coul}} \quad (1)$$

appropriately discretized as outlined in our earlier work.^{3,4} H_{Lutt} is the Luttinger Hamiltonian²³ for the valence bands describing the $\mathbf{k}\cdot\mathbf{p}$ coupling of heavy and light holes; the conduction-band electron is described by a simple parabolic effective-mass expression H_e ; the Coulomb potential W_{Coul} is discretized according to Glutsch, Chemla, and Bechsted.²⁴ The QWR geometry determines the confining potential V_{conf} for electrons and holes. The eigenfunctions of the Hamiltonian (1) have four components corresponding to the hole angular momenta ($J=3/2, m_J = +3/2, +1/2, -1/2, -3/2$); the electron spin can, without loss of generality, be taken as $+1/2$.³

We study as an example so-called V-groove QWRs, which are particular promising for device applications. They result from self-regulated growth with metal-organic chemical vapor deposition (MOCVD) or molecular-beam epitaxy (MBE) on a substrate into which V-shaped grooves were etched. Alternating deposition of GaAs and Al_xGa_{1-x}As (Refs. 25 and 26) or In_xGa_{1-x}As and InP (Refs. 27 and 28) leads to stacks of V-shaped wells and barriers. Due to different growth rates and lateral transport, crescent-shaped thicker well regions develop at the bottom, which act as QWR. The well regions on the side walls will be henceforth referred to as side quantum wells (S-QW). The stack of V-groove QWR is found to be connected by a central region of increased Ga concentration, which will be referred to as vertical quantum well (V-QW). The V-groove QWR geometry is well known from cross-sectional TEM. We use data of Kapon and co-workers for a GaAs/Al_xGa_{1-x}As V-groove QWR with 6.3 nm central thickness grown on a GaAs (001) surface with the

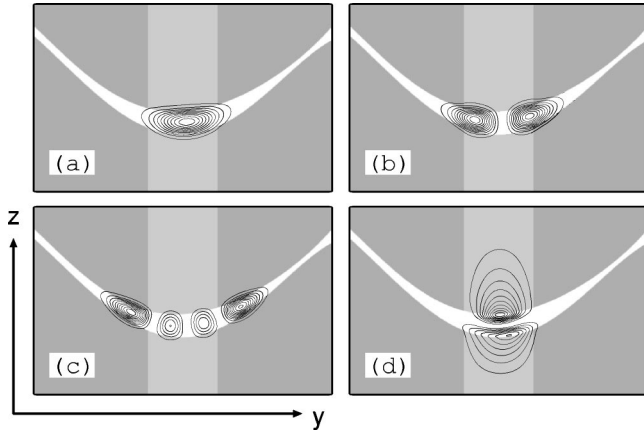


FIG. 1. V-groove GaAs/Al_xGa_{1-x}As quantum wire: Some of the lowest electron-subband states at $k_e = 0.25 \text{ nm}^{-1}$. Each panel shows an area of $50 \text{ nm} \times 80 \text{ nm}$. The shading marks the aluminum concentration $x = 0.33, 0.21,$ and 0.0 in barrier (dark gray), vertical quantum well (light gray), and side quantum well and crescent-shaped wire region (white), respectively.

wire axis (x direction) along $[1\bar{1}0]$.²⁹ Thus, experimental details like a narrowing of the S-QW about 25 nm off the center and a slight left-right asymmetry are included. The latter is specific to the particular sample of the TEM micrograph, but should be representative for asymmetries being present in general. Recent TEM analysis showed that the earlier experiments overestimated the asymmetry state-of-the-art QWR are more symmetric than assumed in the present work.²⁹ The V-QW is described by a vertical slab with Al concentration $x = 0.21$. A more detailed modeling is easily possible within our approach, but seemed not necessary. The geometry of the considered QWR is seen as gray-scale background shading in Figs. 1, 2, and 8 below. The material parameters that were used are summarized in Table I.

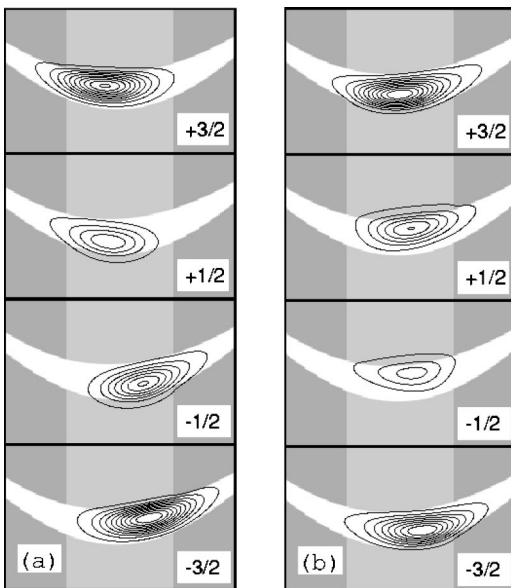


FIG. 2. Probability distribution of the m_J components for the spin-split lowest hole-subband pair at $k_h = 0.25 \text{ nm}^{-1}$. The energy difference is $E(b) - E(a) = 2.5 \text{ meV}$. Panels cover an area of $25 \text{ nm} \times 40 \text{ nm}$.

TABLE I. Overview of the used material parameters; following Ref. 13.

		QWR	barrier	V-QW
Al content	x	0	0.33	0.21
Band gap	E_g (eV)	1.519	1.931	1.781
Luttinger parameters	γ_1	6.790	5.800	6.160
	γ_2	1.924	1.695	1.778
	γ_3	2.681	2.257	2.411
Electron mass	m_e/m_0	0.0665	0.0941	0.0840
Dielectric const.	ϵ	12	12	12
Offset ratio	V_c/V_v	68/32	68/32	68/32

II. NUMERICAL IMPLEMENTATION

Numerical approaches to the exciton in QWR can be classified according to the chosen basis: The exciton wave function is usually discretized in k space, in real space, or it is expanded into a superposition of simpler functions. The latter can be “arbitrary” orbitals with, e.g., Gaussian shape,⁹ or they are derived from single-particle calculations for the subband states. In addition, many groups applied in the past decade variational approaches to QWR excitons, typically using an ansatz with only one or two parameters and considering idealized geometries.

We presented recently full multiband calculations for QW exciton dispersions including $\mathbf{k} \cdot \mathbf{p}$ coupling in real space and compared them to calculations in k space involving a subband expansion.³ The real-space approach to QW spectra was intended as a first step towards the QWR results of the present work. A finite exciton momentum destroys already in the QW case the in-plane rotational invariance. With a resulting matrix dimension $\approx 1.4 \times 10^7$ for grids fine enough to yield well converged results for the exciton dispersion, that method was clearly inferior to a subband expansion in k space. Such an eigenvalue problem can be attacked only if the matrix is sparse and suitable for using efficiently vectorized or parallelized numerical routines.^{30,31}

The advantages of a k -space-based subband expansion, which proved so much more efficient in the QW case, are lost in the QWR case for several reasons: First of all, most technologically important QWR systems such as V-groove QWR, T-shaped QWR,^{32,16} etched mesa structures,^{33,34} and wires grown along natural step-bunched surface steps^{35,36} or etched steps³⁷ show in at least one direction only *weak* confinement. This implies that many subband pairs would have to be taken into account for sufficient accuracy. A further problem are the Coulomb integrals, which have to be calculated and stored for each basis-state pair and each x distance. Coulomb integrals can be obtained more or less analytically only for model systems with rectangular or circular cross section and simple single-particle states. Using such basis states for general, more complicated shapes, however, will lead to poor convergence with basis size. Finally, and maybe even more importantly, the Hamiltonian matrix in a subband expansion is no longer sparse.

The difficulties involved in a QWR exciton calculation are highlighted by the fact that the influence of the valence-band structure on optical properties is treated in the literature almost exclusively on the single-particle level,^{6,10,11,13,38–40}

which is conceptionally and numerically much easier than calculations of the two-particle wave function for the exciton. These publications focus mainly on intersubband absorption and polarization properties, which are considered to be a good test for the one-dimensional character of the involved states.^{33,34}

Numerically very important for calculations at larger momentum along the wire is the choice of the COM coordinate $R_x = \beta x_e + (1 - \beta)x_h$.^{41,1-3} The parameter β relates the particle momenta to the COM momentum Q and the momentum of the relative motion k via

$$k_e = k + \beta Q, \quad k_h = k - (1 - \beta)Q. \quad (2)$$

The better the choice of β is, the less of the oscillating plane-wave factor $\exp(-iQR_x)$ is present in the calculated wave function, and the better is the convergence of the numerical solution. A complete separation of COM motion and relative motion is, however, possible only for parabolic bands and the conventional choice $\beta = m_e/(m_e + m_h)$. In Ref. 3, we showed how to optimize β for general, nonparabolic bands.

III. SINGLE-PARTICLE SUBBANDS

The electron, described by an effective mass that varies with aluminum concentration, see Table I, is the simplest ingredient of our QWR exciton model. Figure 1 presents a selection of electron single-particle states for a momentum $k_e = 0.25 \text{ nm}^{-1}$, which is representative for electrons in the finite-momentum excitons discussed below in Secs. IV and V. Besides ‘‘typical QWR states,’’ Figs. 1(a) and 1(b), also states are seen which are better described as states of the S-QW, Fig. 1(c), or the V-QW, Fig. 1(d). Altogether, a smooth transition from QWR states to QW states is found, which should make electron trapping into the wire region efficient. Due to the heavier electron mass in the $\text{Al}_x\text{Ga}_{1-x}\text{As}$ barriers, effective confinement weakens with increasing electron momentum along the wire, k_e , and the electron envelopes reach deeper into the barriers.

In contrast to the electron, the hole dispersions (not shown) and the corresponding states exhibit some nontrivial features. Probability distributions of the spin components (m_j along the vertical quantization axis z) at finite momentum are shown for the lowest two states in Fig. 2. At vanishing hole momentum, the lowest state is doubly degenerate and the dispersion splits at small, but finite momentum *linearly*. This is equivalent to the valence-subband extrema occurring not at $k_h = 0$, but slightly off. The spin splitting results from the terms of the Luttinger Hamiltonian²³ which are linear in the momentum along the wire axis,

$$H_{\text{Lutt}} = h^{(0)} + k_h h^{(1)} + k_h^2 h^{(2)}. \quad (3)$$

These mix only 3/2 components with 1/2 components:

$$h_{\pm 3/2, \pm 1/2}^{(1)} = \mp 2\sqrt{3}\gamma_3\partial_y, \quad h_{\pm 3/2, \mp 1/2}^{(1)} = \mp 2\sqrt{3}\gamma_2\partial_z. \quad (4)$$

They give a nonzero contribution to the energy only if inversion symmetry is violated, e.g., by the confining potential $V_{\text{conf}}(y, z)$. (The spin splitting is *not* related to the slight deviation from mirror symmetry $y \leftrightarrow -y$.)

The difference in energy goes along with a change of the distribution in real space. In Fig. 2, the components of the

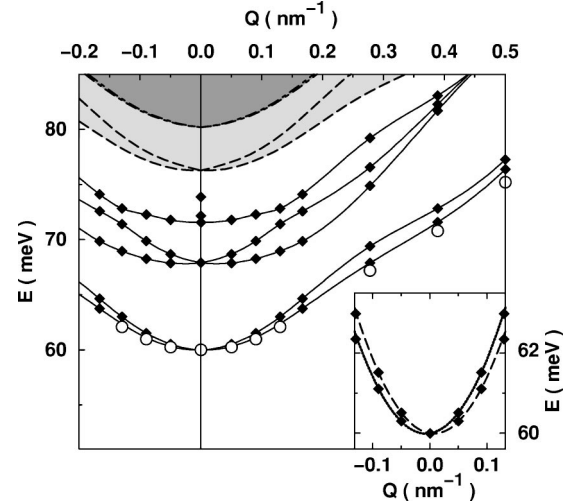


FIG. 3. Dispersion of the lowest exciton states in a V-groove QWR (diamonds). For the lowest ground-state branch, results are shown for the denser mesh as open circles. The exciton continuum edges for the HH_1C_1 pairs (gray, dashed) and the HH_2C_1 pairs (dark-gray, dash-dotted) are included. Inset: The spin-split ground-state dispersion with parabolic fits on an enlarged scale. Note the small linear contribution and the small minimum shifts.

state with lower energy (left panel) penetrate further into the S-QW region; those components with positive m_j are in the ground state displaced to the left, those with negative m_j are displaced to the right. Similar relative displacements of the maxima between corresponding components in Figs. 2(a) and 2(b) are also seen in the vertical direction.

The slight left-right asymmetry of the wire causes a minor additional shift of *all* components to the right. Not surprisingly, the light-hole components $m_j = \pm 1/2$ penetrate further into the V-QW than $m_j = \pm 3/2$ components. Only exactly at $k_h = 0$, eigenstates with strong spin polarization (close to $\pm 3/2$) can be found; for finite k_h , the spin polarization is small. We will find these features for the exciton dispersion and the hole densities within the exciton, too.

IV. EXCITON DISPERSION

Results on exciton energies will be presented for the four-component wave functions on a coarser grid of $N_y \times N_{ye} \times N_{yh} \times N_{ze} \times N_{zh} \times N_x = 4 \times 17^2 \times 17^2 \times 27 \approx 10^7$ and a finer grid of $4 \times 23^2 \times 23^2 \times 27 \approx 3 \times 10^7$ sites for a five-dimensional volume with 57 nm, 37 nm, and 120 nm in the y, z , and x direction, respectively. With these grids, a good accuracy can be obtained if the COM transformation (2) is optimized and a ground-state-adapted discretization²⁴ of the Coulomb potential is used.³ Due to the huge matrix size, we are limited to the very few lowest eigenstates; for the denser grid we are limited to *the* lowest state. In Fig. 3, we show the exciton dispersions for our V-groove QWR.

A spin splitting analogous to that discussed for the hole subbands is clearly seen. It is weak within the lowest doublet (inset of Fig. 3) but large for the next higher doublet. For the lowest doublet, the linear contribution to the dispersion can be obtained from a polynomial fit to the data, with the energy minimum at $Q = 0.007 \text{ nm}^{-1}$. Note that in the exciton Hamiltonian terms linear in Q occur beyond those of Eq. (4).

They result from the quadratic terms $k_h^2 \hbar^{(2)}$ and H_e when the expressions (2) are inserted.

An enlightening discussion of why the lowest doublet is split and why the split is much stronger in T-shaped QWR than in V-groove QWR is given by Goldoni *et al.* in Ref. 10. They note that the HH_1 state of one of the two QWs constituting a T-shaped QWR has a strong LH component from the point of view of the second QW, and vice versa. Hence, the respective HH_1 subbands couple strongly, leading to a strong avoided crossing and a large spin splitting. The argument is formulated for single-particle states there, but applies to excitons as well. We shall point out that, as the present calculation does include the vertical quantum well, one should not be surprised to see in our QWR a feature which has been identified as characteristic for T-shaped wires. However, for this particular QWR, the confinement in the GaAs region is too strong for the V-QW to play a significant role for the ground-state exciton.

The dominant nonparabolicity of the ground-state dispersion in Fig. 3 can be traced back to an avoided crossing near $Q \approx 0.28 \text{ nm}^{-1}$ with higher exciton bands that at $Q=0$ have a strong light-hole component ($m_j = \pm 1/2$). This is not surprising based on similar experience with excitons in bulk⁴¹ and QW (Refs. 1–3) as well as with single-particle hole subbands in QWR.

In the QW case, a comparison of the nonparabolic exciton dispersion with the *electron-hole-pair edge*, or *exciton continuum edge*, $\mathcal{E}_{n_e n_h}(Q)$, proved rather useful.³ It is defined by

$$\mathcal{E}_{n_e n_h}(Q) = \min_{k_e + k_h = Q} \{ \mathcal{E}_{n_e}(k_e) + \mathcal{E}_{n_h}(k_h) \}, \quad (5)$$

and is the minimal kinetic energy of a noninteracting electron-hole pair for a given subband combination $n_e n_h$ and a given Q . This coincides in the independent-subband approximation with the maximal energy of bound excitons for a given subband combination. As in the QW case, the exciton ground-state dispersion is found to follow quite closely the exciton continuum edge, from which it inherits its strong nonparabolicity. Both flatten at higher COM momentum.

The numerical exciton dispersions are reasonably well converged, as the small differences between the results obtained for the two different meshes prove. However, the absolute energies are far from convergence. This is primarily due to the discretization error in the kinetic energy of the electron and, to a lesser extent, the hole. Rigid vertical shifts of up to about 5 meV are included in Fig. 3 and Fig. 4, such that the ground-state excitons (and, in Fig. 4 below, also the shifted continuum edges) coincide at $Q=0$. We stress that the exciton binding energies (difference of exciton energy and continuum edge at given Q) calculated with the two meshes differ only by 0.1 meV (16.2 meV versus 16.3 meV). As an aside, we remark that for a comparable QW of 6.3 nm width with similar material parameters, a binding energy of 10.5 meV is found.³

For an estimation of the Q -dependent numerical uncertainties and in order to show the increase of binding energy with increasing momentum, we display in Fig. 4 the ground-state exciton dispersion on both grids with the vertically displaced continuum edges derived from single-particle subbands calculated on the same grids. We already stated that

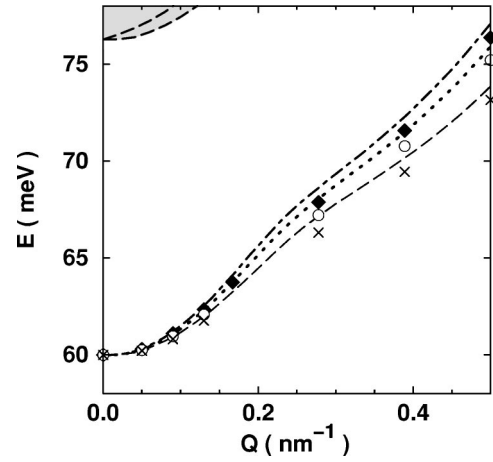


FIG. 4. Comparison of ground-state exciton dispersion on the coarser (diamonds) and the finer mesh (circles) with the vertically displaced exciton continuum edges calculated on the same grids (dot-dashed and dotted, respectively). The fully converged continuum edge (dashed) is vertically displaced for comparison as well as for estimation of the numerical accuracy. Small crosses mark the extrapolation for the exciton dispersion; see text.

the exciton dispersion follows quite closely the exciton continuum edge. The exciton dispersion lies consistently below the appropriately shifted continuum edge. This shows an increase in binding energy with Q , which is almost the same for both grids and is related to the mass increase along the dispersion.³

The exciton dispersion relative to the continuum edge, i.e., the binding energy, seems to be better converged than the continuum edge itself. Since the latter can be obtained with high accuracy as a combination of single-particle properties, we are able to guess where a fully converged exciton dispersion would be (crosses in Fig. 4).

We want to emphasize that, as found before in QW,³ the easily obtainable exciton continuum edge yields a surprisingly reliable guide for the numerically expensive ground-state exciton dispersion. Furthermore, the sign and magnitude of the remaining small deviation can be guessed based on the physical argument of an increasing ground-state exciton binding energy for hole dispersions which become flatter at larger momentum (hole mass and reduced mass increase). The higher excitons follow their respective continuum edges less closely due to strong avoided crossings with other exciton branches (not shown). In particular, the exciton spin splitting within the lowest doublet is at large Q smaller than anticipated based on the difference of the respective continuum edges.

V. EXCITON WAVE FUNCTIONS

Figure 5 shows the multicomponent character of the ground-state exciton wave function near the origin as well as at a COM momentum close to the avoided-crossing region. A strong admixture of light-hole states ($m_j = \pm 1/2$) is seen for the larger Q . The light-hole contribution increases further for even larger COM momenta, as shown in Fig. 6. Note that this is only in part due to mixing of LH_1C_1 and HH_1C_1 excitons; the lowest hole subband (HH_1) itself acquires a

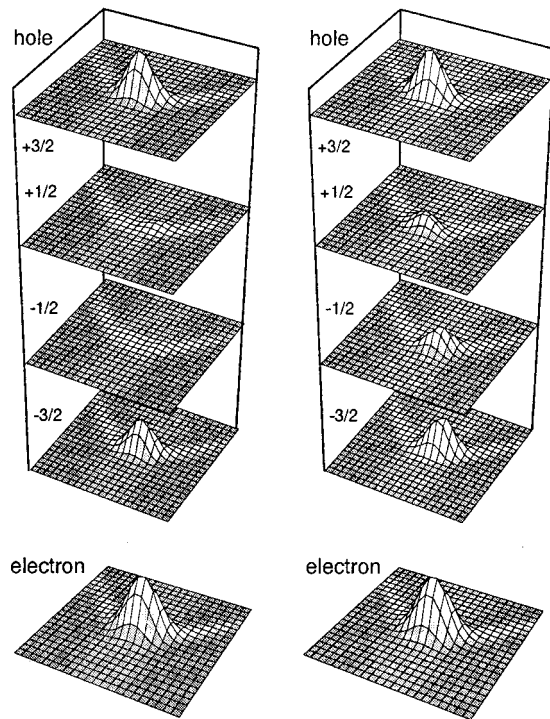


FIG. 5. Ground-state exciton for $Q=0.09 \text{ nm}^{-1}$ (left) and $Q=0.28 \text{ nm}^{-1}$ (right). Hole densities for the different m_J components as well as the electron density are shown on $37 \text{ nm} \times 57 \text{ nm}$ areas.

strong contribution of ‘‘bulk light-hole states,’’ i.e., $m_J = \pm 1/2$ components; see Fig. 2.

For a more detailed analysis of the internal structure of the exciton with increasing momentum, we display in Fig. 7 the exciton extension along all five coordinates. For each one of these, the squared wave function was summed over the remaining four directions and the angular momentum components. Then, the root-mean-square deviation was calculated. The strong confinement of electron and hole along the growth direction, z , is clearly seen; confinement is weaker in the S-QW direction y . The largest extension is that of the relative motion along the wire (x direction). With increasing COM momentum, the hole in the exciton can relax in the weakly confined direction. However, the exciton contracts at the same time along the wire axis. The latter change is stronger, suggesting a slight enhancement of the exciton binding energy with Q , in agreement with the discussion of Figs. 3, 4, and similar to the results in comparable QW. The density profiles in the yz plane (not shown) can be fitted well by

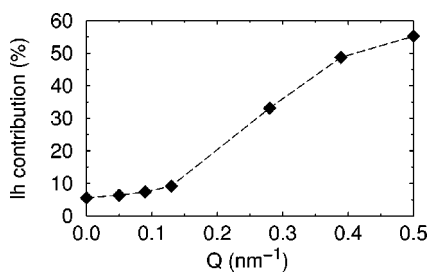


FIG. 6. Contribution of bulk light-hole states ($m_J = \pm 1/2$) to the exciton ground-state versus COM momentum Q .

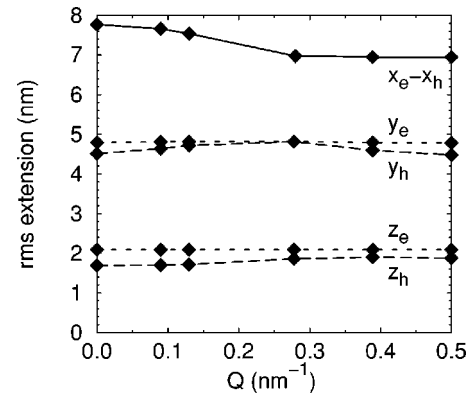


FIG. 7. Spatial extension (root-mean-square) of the exciton ground-state along each dimension versus COM momentum Q .

Gaussian functions. For density profiles along the wire, see the discussion of Fig. 8, below.

On the coarser mesh, higher exciton states can be obtained as well. Their hole densities and relative wave function along the wire are shown in Fig. 8. For their description, we use a notation like HH_2C_1-s , which states, e.g., that this particular exciton branch is at $Q=0$ derived from the second QWR hole subband which has primarily heavy-hole ($m_J = \pm 3/2$) character and from the lowest electron subband; along the wire axis, the dominant component(s) have no nodes and therefore resemble an s state.

The two states of Fig. 8(b) which lie above the ground-state doublet [Fig. 8(a) with clear HH_1C_1-s character] have one node in the S-QW direction. They can be interpreted as originating from a heavy-hole state with one node, and are thus HH_2C_1-s states. The next doublet, Fig. 8(c), has one node along the wire, resembling a p state. As it has no nodes in the yz plane for both electron and hole coordinate, it is a HH_1C_1-p doublet. Note its much larger extension in wire direction compared to the s states, which goes along with an increased size in the S-QW direction, at least in comparison to the s state of the same subband pair, Fig. 8(a).

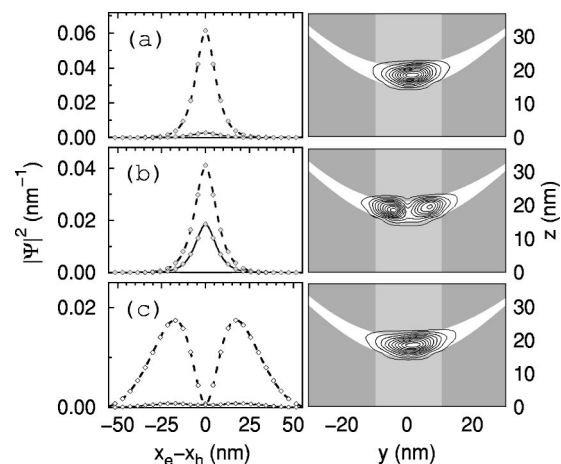


FIG. 8. Right: Hole densities in the yz plane. Left: Density of the relative wave-function components (dashed: heavy hole $m_J = \pm 3/2$; solid: light hole $m_J = \pm 1/2$) along the wire for the lowest three doublets at $Q=0$. From top to bottom: HH_1C_1-s , HH_2C_1-s , HH_1C_1-p . Lines are hyperbolic-secant fits in panels (a) and (b), and spline fits in (c) to the numerical data (diamonds).

TABLE II. Kinetic COM mass for the ground-state HH_1C_1-s exciton derived from fits of the dispersion in the range $Q < 0.1 \text{ nm}^{-1}$ and from expression (7). In parentheses: mass from extrapolated dispersion of Fig. 4. Quantum-well data are from calculations based on Ref. 3.

M_X/m_0	QWR	5 nm QW	10 nm QW
$Q < 0.1 \text{ nm}^{-1}$	0.27 (0.33)	0.31	0.32
Eq. (7)	0.28	0.29	0.31

The relative motion in wire direction is determined by the Coulomb interaction, modified by form factors. In analogy to two-dimensional results, a wave function shape between an exponential and a Gaussian is expected and is seen in Figs. 8(a) and (b), indeed. The large-distance behavior is approximately exponential; at small distances, the relative wave function does not show a cusp, because the effective Coulomb interaction is weakened there. For the ground state, a hyperbolic-secant function fits the squared wave function almost perfectly.

This brings us to the question of how closely the exciton ground-state wave function can be approximated by a factorization ansatz of the form

$$\Psi_{\text{gs}} \approx \varphi_{\text{rel}}(x_e - x_h) \varphi_e(y_e, z_e) \varphi_h(y_h, z_h) \chi_0, \quad (6)$$

with suitably chosen functions φ_e, φ_h as effective single-particle electron and hole wave functions in the confined directions and φ_{rel} for the relative motion along the wire, and with a spatially constant four-component vector χ_0 . Having the numerical exciton wave function at hand, this can be easily answered. At a not too large momentum of $Q = 0.09 \text{ nm}^{-1}$ (see left panel of Fig. 5) an overlap of 94% between the factorized ansatz Eq. (6) and the numerically exact result can be obtained if only the $m_j = \pm 3/2$ components are included with equal weight, $\chi_0 = (1/\sqrt{2}, 0, 0, -1/\sqrt{2})$. This is rather high, especially in view of the fact that in Ritz's variational principle, eigenvalue errors are proportional to the *square* of the wave-function deviation. The inclusion of $m_j = \pm 1/2$ components, which is needed for larger Q , increases the overlap only to 95%. Finally, we come back to two subjects already mentioned, the kinetic COM mass and the polarization properties of excitonic luminescence.

VI. KINETIC EXCITON MASS

The concept of a kinetic COM mass for a nonparabolic dispersion depends on the momentum range that is considered. In Table II, some values of a kinetic COM mass for the ground-state exciton in the considered QWR and in QWs with 5 and 10 nm well width are compiled. The QW widths correspond roughly to the range of wire z widths, taking into account that the lower Al concentration in the V-QW weakens the confinement compared to GaAs/ $\text{Al}_{0.33}\text{Ga}_{0.67}\text{As}$ QWs. Because the QW and QWR dispersions are strongly nonparabolic, average values derived from parabolic fits to the dispersion in a Q range of about the inverse Bohr radius ($Q < 0.1 \text{ nm}^{-1}$) are reported. This part of the dispersion is the one expected to play a dominant role in exciton localization.

Included in Table II are also the results of a simple approximate expression for the exciton mass which we have derived and tested before in Ref. 3. It gives an estimate for the exciton's kinetic mass in the same Q range, which is obtained from the single-particle subband dispersions $\epsilon_{e,h}(k)$ weighted with the squared Fourier transform $\Psi_{Q=0}(k)$ of the exciton wave function at vanishing COM momentum Q . Within the factorization approximation, Eq. (6), only the Fourier transform $\tilde{\varphi}_{\text{rel}}(k_x)$ is important, and the mass formula reads

$$M_X = m_e + m_h \quad \text{with}$$

$$\frac{1}{m_{e,h}} = \frac{1}{\hbar^2} \int dk_x |\tilde{\varphi}_{\text{rel}}(k_x)|^2 \frac{\partial^2}{\partial k_x^2} \epsilon_{e,h}(k_x). \quad (7)$$

The Luttinger parameters of Table I yield in the spherical approximation for the bulk heavy-hole mass $m_h/m_0 = (\gamma_1 - 4\gamma_2/5 - 6\gamma_3/5)^{-1} = 0.49$, thus $m_e + m_h = 0.56m_0$. A decrease of the exciton mass going from GaAs bulk to GaAs/ $\text{Al}_x\text{Ga}_{1-x}\text{As}$ QW can be understood as a result of the heavy- and light-hole separation due to confinement. For QWR, we find a mass of $0.33m_0$. The agreement of the simple expression (7) with the result of the full numerical calculation is not as good for the QWR case as for QWs. We attribute this to a stronger momentum dependence of the exciton's internal structure, probably reflecting the smaller subband separations and the linear terms in the dispersions.

VII. POLARIZATION ANISOTROPY

The exciton wave functions can be used for the calculation of the polarization anisotropy of excitonic luminescence and absorption. Results on the polarization dependence in V-groove wires are known from experiments^{42,12} and from single-particle calculations.^{10,13} The average anisotropy at the onset of the electron-hole continuum in the single-particle approximation should be comparable to our exciton calculations. References 12 and 13 give an average anisotropy value of 10%, whereas Refs. 42 and 10 state 10–20% for various V-groove QWR samples of different geometry.

For the relative absorption strength, as given by the squared momentum matrix element averaged over the ground-state doublet (corresponding to the different electron spin states),

$$a_j = \frac{1}{2} \sum_{\pm} |\langle 0 | \hat{p}_j | \Psi_{\text{gs}}^{(\pm)} \rangle|^2, \quad j = x, y, x, \quad (8)$$

we find the following values:

$$\frac{a_x - a_y}{a_x + a_y} = 0.12, \quad \frac{2a_z}{a_x + a_y} = 0.01. \quad (9)$$

This confirms what one would expect based on the single-particle results, e.g., combining the upper left corners of Figs. 1 and 2. Absorption with light polarized along z involves only the $m_j = \pm 1/2$ components, which according to Fig. 6 are weak for Q values corresponding to photon momenta. In contrast, light polarized in the xy plane is absorbed mainly by the $m_j = \pm 3/2$ components. The polarization de-

pendence perpendicular to the growth direction is due to the weak, but noticeable, extra confinement in the y direction.

The calculated absorption anisotropy is in good agreement with the experimental results. The fact that the single-particle results of Refs. 10 and 13 are so close to Eq. (9) is probably due to the high overlap of the exciton wave function with the factorized form Eq. (6), which in turn reflects the strong carrier confinement in V-groove QWR.

VIII. SUMMARY

In summary, we have shown that multiband QWR exciton calculations in real space are feasible. Results for exciton dispersion, wave-function character, and kinetic COM mass were found to be quite close to those derivable from the exciton continuum edge, a factorization ansatz, and the mass estimate of Eq. (7), respectively. The calculated polarization anisotropy agrees well with experimental data.

As an outlook, we would like to list some physical properties that can be obtained from similar calculations of the ground-state exciton or the lowest exciton doublet at finite COM momentum: We already mentioned in the Introduction

the possible application of QWR in lasers. For their modeling, optical transition matrix elements and the density of states are needed. The exciton dispersion also enters the polariton dispersion.¹ Exciton localization involves COM wave functions, which in turn can be obtained by a COM Schrödinger equation that needs the ground-state dispersion or at least the exciton mass as input.²² The same is true for relaxation processes and diffusion. The quantum confined Stark effect in QWR (Refs. 14, 43, and 44) and experiments in magnetic fields^{45,46} can be treated by inclusion of the appropriate terms in the Hamiltonian.

ACKNOWLEDGMENTS

We wish to thank R. Zimmermann, Berlin, as well as M.-A. Dupertuis and C. Vanderstraeten, Lausanne, for valuable contributions. This work has been funded by the Deutsche Forschungsgemeinschaft in the frame of SFB 296. We gratefully acknowledge support by the Rechenzentrum of the Humboldt University and the Konrad-Zuse-Zentrum in Berlin, in particular through access to their Cray J932 (project bvph08as).

-
- ¹S. Jorda, U. Rössler, and D. Broido, *Phys. Rev. B* **48**, 1669 (1993).
- ²A.L.C. Triques and J.A. Brum, *Phys. Rev. B* **56**, 2094 (1997).
- ³A. Siarkos, E. Runge, and R. Zimmermann, *Phys. Rev. B* **61**, 10 854 (2000).
- ⁴A. Siarkos, E. Runge, and R. Zimmermann, *Ann. Phys. (Leipzig)* **7**, 523 (1998).
- ⁵L. Banyai, I. Galbraith, C. Ell, and H. Haug, *Phys. Rev. B* **36**, 6099 (1987).
- ⁶F. Rossi and E. Molinari, *Phys. Rev. B* **53**, 16 462 (1996).
- ⁷S. Glutsch, F. Bechstedt, W. Wegscheider, and G. Schedelbeck, *Phys. Rev. B* **56**, 4108 (1997).
- ⁸S.N. Walck, T.L. Reinecke, and P.A. Knipp, *Phys. Rev. B* **56**, 9235 (1997).
- ⁹J.-B. Xia and K.W. Cheah, *Phys. Rev. B* **55**, 1596 (1997).
- ¹⁰G. Goldoni, F. Rossi, E. Molinari, and A. Fasolino, *Phys. Rev. B* **55**, 7110 (1997).
- ¹¹O. Stier and D. Bimberg, *Phys. Rev. B* **55**, 7726 (1997).
- ¹²F. Vouilloz, D.Y. Oberli, M.-A. Dupertuis, A. Gustafsson, F. Reinhardt, and E. Kapon, *Phys. Rev. Lett.* **78**, 1580 (1997).
- ¹³F. Vouilloz, D.Y. Oberli, M.-A. Dupertuis, A. Gustafsson, F. Reinhardt, and E. Kapon, *Phys. Rev. B* **57**, 12 378 (1998).
- ¹⁴S. Benner and H. Haug, *Phys. Rev. B* **47**, 15 750 (1993).
- ¹⁵M. Grundmann, O. Stier, and D. Bimberg, *Phys. Rev. B* **58**, 10 557 (1998).
- ¹⁶W. Wegscheider, L.N. Pfeiffer, M.M. Dignam, A. Pinczuk, K.W. West, S.L. McCall, and R. Hull, *Phys. Rev. Lett.* **71**, 4071 (1993).
- ¹⁷R. Ambigapathy, I. Bar-Joseph, D.Y. Oberli, S. Haacke, M.J. Brasil, F. Reinhardt, E. Kapon, and B. Deveaud, *Phys. Rev. Lett.* **78**, 3579 (1997); L. Sirigu, D. Y. Oberli, D. Degiorgi, A. Rudra, and E. Kapon, *Phys. Rev. B* **61**, 10 575 (2000).
- ¹⁸T. Ogawa and T. Takagahara, *Phys. Rev. B* **44**, 8138 (1991).
- ¹⁹S. Glutsch and F. Bechstedt, *Phys. Rev. B* **47**, 4315 (1993).
- ²⁰F. Rossi and E. Molinari, *Phys. Rev. Lett.* **76**, 3642 (1996).
- ²¹A.L. Ivanov and H. Haug, *Phys. Rev. Lett.* **71**, 3182 (1993).
- ²²E. Runge and R. Zimmermann, *Festkoerperprobleme* **38**, 251 (1998).
- ²³J.M. Luttinger, *Phys. Rev.* **102**, 1030 (1956).
- ²⁴S. Glutsch, D.S. Chemla, and F. Bechstedt, *Phys. Rev. B* **54**, 11 592 (1996).
- ²⁵E. Kapon, M.C. Tamargo, and D.M. Hwang, *Appl. Phys. Lett.* **50**, 347 (1989).
- ²⁶E. Kapon, D.M. Hwang, and R. Bhat, *Phys. Rev. Lett.* **63**, 430 (1989).
- ²⁷J. Wang, B.J. Robinson, D.A. Thompson, and J.G. Simmons, *Appl. Phys. Lett.* **67**, 2358 (1995).
- ²⁸M. Kappelt, M. Grundmann, A. Krost, V. Türck, and D. Bimberg, *Appl. Phys. Lett.* **68**, 3596 (1996).
- ²⁹M. A. Dupertuis (private communication).
- ³⁰U. Elsner, V. Mehrmann, F. Milde, R.A. Römer, and M. Schreiber, *SIAM (Soc. Ind. Appl. Math.) J. Sci. Stat. Comput.* **20**, 2089 (1999).
- ³¹The highly efficient eigenvalue package ARPACK based on the implicitly restarted Arnoldi method and its parallel version PARPACK can be downloaded free of charge at <http://www.caam.rice.edu/software>.
- ³²A.R. Goñi, L.N. Pfeiffer, K.W. West, A. Pinczuk, H.U. Baranger, and H.L. Störmer, *Appl. Phys. Lett.* **61**, 1956 (1992).
- ³³M. Kohl, D. Heitmann, P. Grambow, and K. Ploog, *Phys. Rev. Lett.* **63**, 2124 (1989).
- ³⁴P. Ils, Ch. Greus, A. Forchel, V.D. Kulakovskii, N.A. Gippius, and S.G. Tikhodeev, *Phys. Rev. B* **51**, 4272 (1995).
- ³⁵R. Nötzel, N.N. Ledentsov, L. Däweritz, K. Ploog, and M. Hohenstein, *Phys. Rev. B* **45**, 3507 (1992).
- ³⁶I. Rasnik, L.G.C. Rego, M.V. Marquezini, A.L.C. Triques, M.J.S.P. Brasil, J.A. Brum, and M.A. Cotta, *Phys. Rev. B* **58**, 9876 (1998).
- ³⁷R. Nötzel, U. Jahn, Z. Niu, A. Trampert, J. Fricke, H.-P. Schönherr, T. Kurth, D. Heitmann, L. Däweritz, and K.H. Ploog,

- Appl. Phys. Lett. **72**, 2002 (1998).
- ³⁸P.C. Sercel and K.J. Vahala, Phys. Rev. B **44**, 5681 (1991).
- ³⁹D.S. Citrin and Y.-C. Chang, Phys. Rev. B **43**, 11 703 (1991).
- ⁴⁰U. Bockelmann and G. Bastard, Phys. Rev. B **45**, 1688 (1992).
- ⁴¹M. Altarelli and N.O. Lipari, Phys. Rev. B **15**, 4898 (1977).
- ⁴²G. Goldoni, F. Rossi, E. Molinari, A. Fasolino, R. Rinaldi, and R. Cingolani, Appl. Phys. Lett. **69**, 2965 (1996).
- ⁴³K. Chang and J.B. Xia, Phys. Rev. B **58**, 2031 (1998).
- ⁴⁴M. A. Dupertuis, E. Martinet, H. Weman, and E. Kapon, Europhys. Lett. **44**, 759 (1998).
- ⁴⁵G. Goldoni and A. Fasolino, Phys. Rev. B **52**, 14 118 (1995).
- ⁴⁶S.N. Walck and T.L. Reinecke, Phys. Rev. B **57**, 9088 (1998).